Spatially displaced excitation contributes to the encoding of interrupted motion by the retinal direction-selective circuit

Jennifer Ding[1,2], Albert Chen[3], Janet Chung[2], Hector Acaron Ledesma[4], David M. Berson[5], Stephanie Palmer[1,3,6]*, Wei Wei[1,2,6]*

1. Committee on Neurobiology Graduate Program, The University of Chicago
2. Department of Neurobiology, The University of Chicago
3. Department of Organismal Biology, The University of Chicago
4. Graduate Program in Biophysical Sciences, The University of Chicago
5. Department of Neuroscience and Carney Institute for Brain Science, Brown University
6. Grossman Institute for Neuroscience, Quantitative Biology and Human Behavior, The University of Chicago

*Co-corresponding authors: weiw@uchicago.edu; sepalmer@uchicago.edu

Abstract

Spatially distributed excitation and inhibition collectively shape a visual neuron's receptive field (RF) properties. In the direction-selective circuit of the mammalian retina, the effects of strong null-direction inhibition of On-Off direction-selective ganglion cells (ON-OFF DSGCs) on their direction selectivity are well-studied. However, how excitatory inputs influence the On-Off DSGC's visual response is underexplored. Here, we report that the glutamatergic excitation of On-Off DSGCs shows a spatial displacement to the side where preferred-direction motion stimuli approach the soma (the 'preferred side'). Underlying this displacement is a non-uniform distribution of excitatory conductance across the dendritic span of the DSGC on the preferred-null motion axis. The skewed excitatory RF contributes to robust null-direction spiking during RF activation limited to the preferred side, a potential ethologically relevant signal to encode interrupted or discontinuous motion trajectories abundant in natural scenes. Theoretical analysis indicates that such differential firing patterns of On-Off DSGCs to continuous and interrupted motion stimuli may help leverage synchronous firing to signal the spatial location of a moving object in complex, naturalistic visual environments. Our study highlights that visual circuitry, even the well-defined direction-selective circuit, exploits different sets of neural mechanisms under different stimulus conditions to generate context-dependent neural representations of visual features.

Introduction

How do sensory systems convert sensory inputs into behaviorally relevant neural signals? This question has been extensively investigated in the early visual system, where a neuron's responses to a set of parameterizable visual stimuli can be systematically probed to reveal a cell's receptive field (RF) properties in space and time. It has been increasingly appreciated that context-dependent neural mechanisms dynamically shape neuronal RFs even at the earliest stage of visual processing in the retina. The transformation from the visual input to a retinal ganglion cell's spiking output is influenced by spatiotemporal patterns of stimuli in both the RF center and surround regions, highlighting the necessity of using diverse, ethologically relevant visual stimuli for delineating RF properties and for ultimately understanding neural coding of the animal's natural environment (Chiao and Masland, 2003; Demb et al., 1999; Deny et al., 2017; Huang et al., 2019; Ölveczky et al., 2003; Takeshita and Gollisch, 2014; Turner et al., 2018).

Direction-selective ganglion cells (DSGCs) in the mammalian retina are well-studied for their motion direction selectivity. A DSGC fires maximally to visual stimuli moving across its RF in its preferred direction and is inhibited from firing by stimuli moving in the opposite, null direction (Barlow and Hill, 1963; Barlow and Levick, 1965). The direction-selective spiking of the DSGC is largely attributed to the strong null-direction inhibition that the DSGC receives from the starburst amacrine cell (SAC) (Briggman et al., 2011; Euler et al., 2002; Fried et al., 2002; Lee and Zhou, 2010; Taylor and Vaney, 2002; Wei et al., 2011; Yonehara et al., 2011). The most studied DSGC type, the On-Off DSGC, prefers motion in one of the four cardinal directions (Oyster and Barlow, 1967; Sabbah et al., 2017). They have bistratified dendritic arbors in the On and Off sublamina of the inner plexiform layer (IPL) to extract motion directions of bright and dark signals, respectively (**Figure 1A**) (Famiglietti 1983; He and Masland, 1998; Kittila and Massey, 1997).

The RF of On-Off DSGCs has been studied with conventional visual stimuli such as stationary and moving spots, bars, and gratings. For motion stimuli that traverse across the entire RF, On-Off DSGC responses remain direction-selective over a broad range of contrast, luminance, speed, and background noise levels (Barlow and Levick, 1965; Chen et al., 2016; Grzywacz and Amthor, 2007; Lipin et al., 2015; Sethuramanujam et al., 2016; Sivyer et al., 2010). However, motion stimuli restricted to the distal RF subregion on the preferred side (defined as the side from which the preferred-direction moving stimulus approaches the RF) can elicit non-directional firing (He et al., 1999; He and Masland, 1998; Rivlin-Etzion et al., 2011; Trenholm et al., 2011). Based on the responses to moving stimuli presented to different subregions of the DSGC RF, the cell's RF structure can be viewed as consisting of multiple 'DS

subunits' and a 'non-DS zone' at the edge of the preferred side. However, the neural mechanisms underlying the modular and heterogenous RF subunits of On-Off DSGCs have not been elucidated. Furthermore, the functional significance of this fine RF structure is not clear.

In this study, we investigated the spatial RF structure of the mouse On-Off DSGC subtype that prefers motion in the posterior direction of the visual field (pDSGC). We found that the pDSGC spiking RF is skewed towards the preferred side of the cell for both stationary and moving stimuli, even in the absence of SAC-mediated inhibition. Combining anatomical and functional analyses, we found a spatially non-uniform glutamatergic excitatory conductance that contributes to this spatial displacement. As a result of the displaced RF, moving stimuli that only activate the preferred side of the pDSGC RF trigger robust firing during either preferred or null direction motion. Theoretical analyses of the On-Off DSGC population response allow us to speculate about the ethological relevance of the displaced RF in processing complex natural scenes, suggesting that it can allow for better estimation of object location when a moving object emerges from behind an occluder. We term this type of motion 'interrupted motion' to distinguish it from more standard constant motion stimuli. This phenomenon might also allow synchronous firing from different subtypes of DSGCs to serve as a useful alarm signal in complex scenes.

Results

Glutamatergic excitation of the On-Off pDSGC is spatially asymmetric relative to the soma

To investigate the spatial distribution of excitatory inputs to On-Off pDSGCs, we targeted pDSGCs in the Drd4-GFP transgenic mouse line to record their On spiking and synaptic responses to the light onset of flashing stationary bright spots presented to the periphery of the DSGC RF. These spots were 110 μm in diameter and centered 165 μm from the soma of the recorded DSGC (**Figure 1B**, schematic). Measurement of the average radius of pDSGC On dendrites (88.1, SEM 13.9 μm, from 25 cells, see Methods) indicates that the spot mostly covered areas beyond the dendritic span of these cells. For each cell tested, we also presented a moving bar stimulus to confirm its directional tuning to posterior-direction motion in the visual field.

The spot stimulus delivered to the pDSGC RF periphery uncovered an asymmetric RF organization: the maximal spiking was triggered by the spot shown on the preferred side of the cell, and the minimal response was triggered to the spot shown on the null side (**Figure 1B**), indicating a spatial displacement of this aspect of the RF relative to the soma. To quantify the extent of this RF displacement, we calculated a

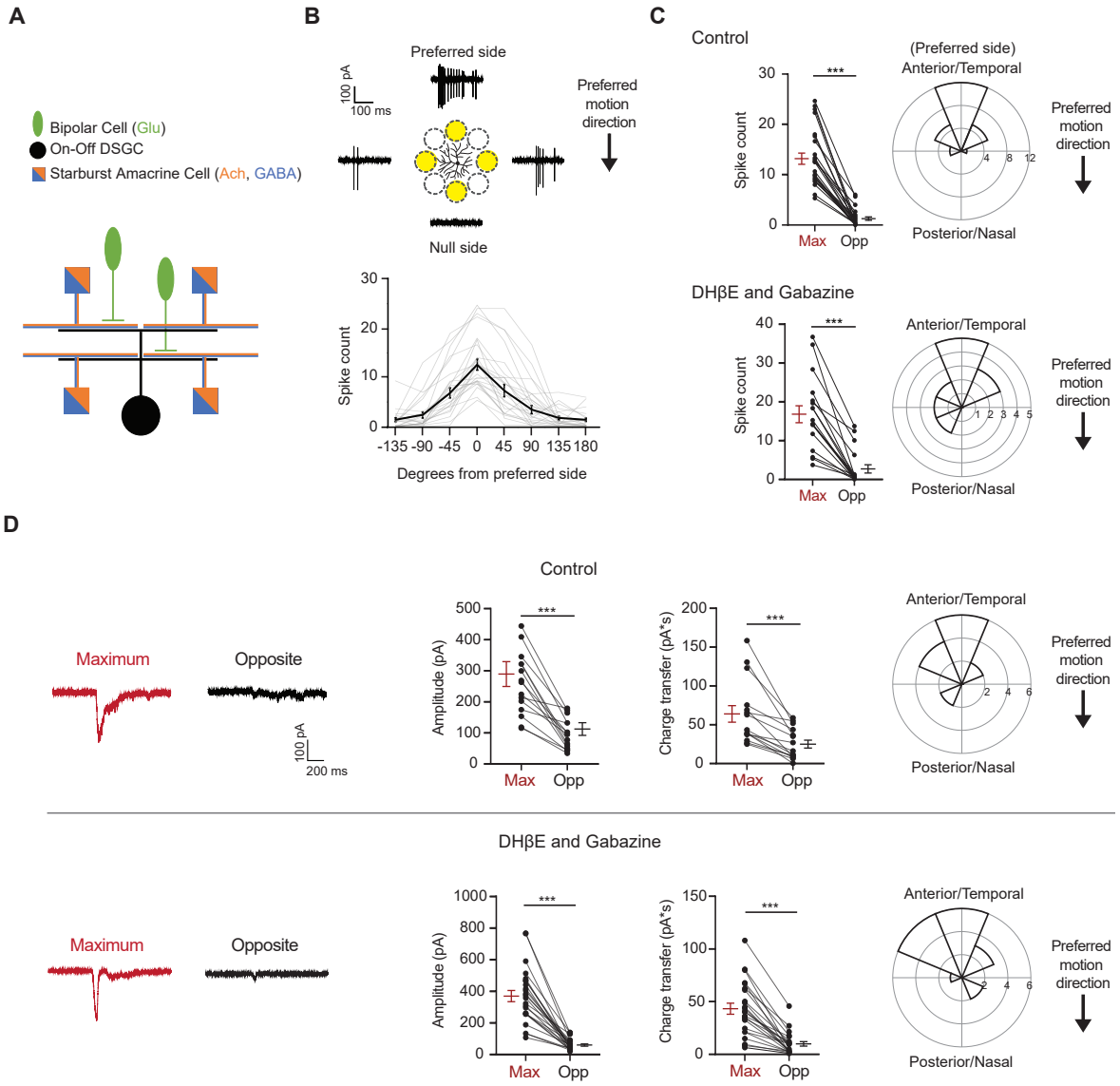

Figure 1. Drd4-GFP labeled pDSGCs have spatially asymmetric glutamatergic receptive fields.

(A) Schematic showing types of presynaptic neurons to an On-Off DSGC and the neurotransmitters they use. **(B)** Top: Example On spiking responses of a pDSGC to four different peripheral spots presented around dendritic span. Bottom: Individual (gray) and mean (black) pDSGC On spike counts evoked by spots presented at different locations (25 cells). **(C)** Top left: Pairwise comparison of mean spike counts in regions evoking the maximum number of spikes (Max) and the opposite region (Opp) in the control condition (25 cells). Top right: Polar histogram of Max region locations aligned to the preferred-null motion axis. Radius indicates number of cells. Bottom: Same as in top but experiments performed in DHβE + Gabazine (18 cells). **(D)** Left: Example On EPSC responses to spots shown in the regions evoking the strongest EPSCs (Max) and the opposite region (Opp) in control (top) and in DHβE + Gabazine (bottom). Middle: Pairwise comparisons of EPSC amplitude and charge transfer to spots presented in the Max region and Opp region (Control: 15 cells; DHβE + Gabazine: 24 cells). Right: Polar histograms of Max region locations determined by EPSC charge transfer aligned to the preferred-null motion axis. Radius indicates number of cells. Summary statistics are mean ± SEM, ***p < 0.001.

142 region selectivity index (RSI) defined as the normalized difference of the maximum
143 response (Max) and the response to the spot presented in the opposite region (Opp)
144 (see Methods). pDSGCs exhibit a robust spatial bias of their spiking RFs to the
145 preferred side (**Figures 1C** "Control" and **S1A**).
146
147 Because a well-documented asymmetry in the direction-selective circuit is the
148 asymmetric inhibition from SACs to DSGCs, we next tested whether the displacement
149 of the pDSGC spiking RF is eliminated by blocking SAC inputs. We perfused the retina
150 with the nicotinic antagonist DHβE and the $GABA_A$ receptor antagonist gabazine to
151 block these inputs. Under this condition, we still observed a spatial asymmetry in
152 pDSGC spiking activity evoked by the flashing spots (**Figures 1C, S1A and S1B**,
153 "DHβE and Gabazine"), indicating a spatial displacement of glutamatergic excitation of
154 the pDSGC in the absence of SAC influence.
155
156 To directly measure the strength of excitatory inputs to pDSGCs at different
157 stimulus locations, we performed whole-cell voltage clamp recordings of excitatory
158 postsynaptic currents (EPSCs) evoked by peripheral flashing spots. Consistent with the
159 pattern of pDSGC spiking activity, spot-evoked EPSCs show a spatial bias towards the
160 preferred side (**Figures 1D and S1C**, "Control"). Isolation of the glutamatergic
161 component of the EPSC by the addition of DHβE and gabazine confirms the persistence
162 of the spatial asymmetry, indicating that the glutamatergic excitation of the pDSGC is
163 not isotropic but is spatially displaced relative to the soma (**Figures 1D, S1B and S1C**,
164 "DHβE and Gabazine"). This pharmacological manipulation also rules out potential
165 confounding influences of asymmetric inhibitory inputs from SACs on pDSGC EPSCs
166 during voltage clamp recordings due to space clamp.
167
168 We investigated the Off responses in tandem with the On responses and found
169 the same RF displacement in all conditions (**Figures S1D and S1F**). We focused on the
170 On response for the remaining experiments.
171
172 **Non-uniform excitatory conductance across the preferred-null motion axis**
173 **contributes to the asymmetric glutamatergic RF**
174
175 An asymmetric excitatory RF of a retinal neuron may result from asymmetric
176 dendritic arbors and/or an asymmetric distribution of excitatory synaptic inputs across its
177 dendritic field. To examine the relationship between pDSGC dendritic morphology and
178 glutamatergic inputs, we performed two-photon imaging of dye-filled dendritic arbors
179 after recording glutamatergic EPSCs evoked by the peripheral flashing spot stimulus
180 described above (**Figures 2A and 2B**). Consistent with previous studies, On dendritic
181 arbors of pDSGCs do not exhibit a salient or consistent bias relative to the cell's
182 preferred motion direction. The total dendritic length or the number of dendritic

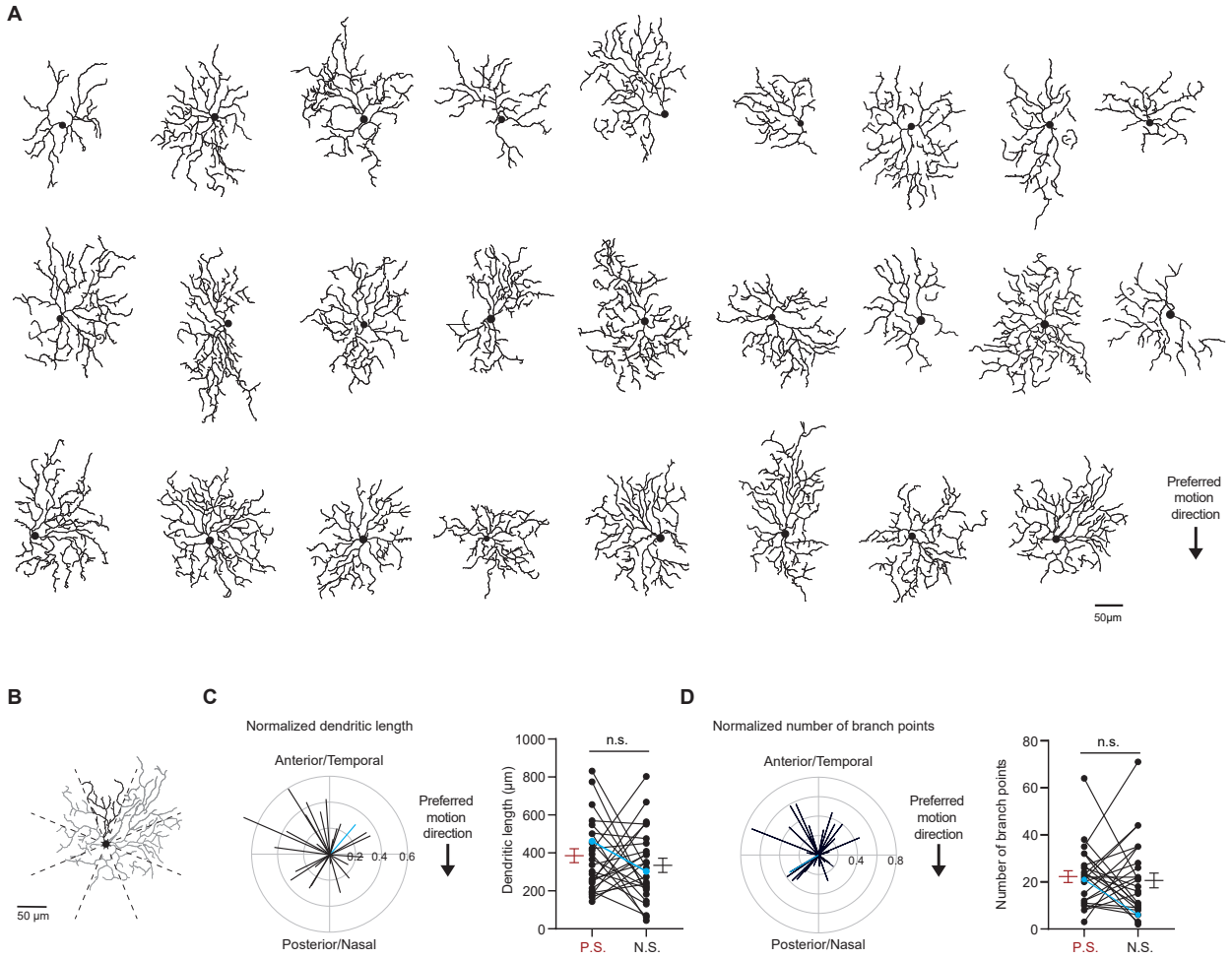

Figure 2. pDSGC dendritic morphology does not show a spatial bias towards the preferred side.

(A) Traced On layer dendritic morphologies of pDSGCs aligned to their preferred-direction motion. **(B)** Example morphology of a pDSGC cell divided into eight sectors for calculating normalized dendritic length vector. **(C)** Left: Normalized vector sum of dendritic length aligned to pDSGCs' preferred direction motion. Right: Pairwise comparison of dendritic length on the preferred vs null sides of each cell (26 cells, $p = 0.51$). Blue represents example cell in **B**. **(D)** Left: Normalized vector sum of branch points aligned to pDSGCs' preferred direction motion. Right: Pairwise comparison of branch points on the preferred vs null side (26 cells, $p = 0.68$). Blue represents example cell in **B**. Summary statistics are mean ± SEM.

197 branching points does not significantly differ between the preferred and null sides of the
198 pDSGC dendritic field (**Figures 2C, 2D and S2A**). This apparent randomness of
199 dendritic arbor distribution relative to the cell's preferred motion direction contrasts with
200 the previously reported mouse On-Off DSGC subtype preferring motion in the superior
201 direction that have dendritic arbors strongly displaced to the null side of the soma (Kay
202 et al., 2011; Trenholm et al., 2011).
203
204 Although pDSGC dendritic fields are not strongly skewed towards the preferred
205 side of the soma, a quantitative comparison between pDSGC dendritic arbor distribution
206 and the distribution of their glutamatergic EPSCs has not been performed. We found a
207 non-random skew of the pDSGC dendritic length and number of branch points towards
208 the regions corresponding to spots evoking the strongest glutamatergic EPSCs (**Figure**
209 **S2B**). However, this structural bias is not correlated with the bias in EPSC strength
210 (**Figure S2C**), suggesting that dendritic arbor density alone cannot fully explain the
211 displacement of the pDSGC glutamatergic RF.
212
213 To further explore the relationship between the pDSGC glutamatergic RF and its
214 dendritic distribution, we performed another set of experiments to obtain a more
215 complete RF map. First, the preferred direction of each cell's spiking activity was
216 determined by loose cell-attached recordings using a moving bar stimulus with no
217 synaptic blockers. Next, peripheral flashing spots were used to estimate the spatial
218 displacement of the pDSGC glutamatergic RF in the presence of nicotinic and
219 GABAergic receptor antagonists (DHβE + Gabazine) as described above. Then, a
220 smaller, 20 μm diameter bright stationary spot was repeatedly flashed at random
221 locations within a 11-by-11 220 μm square grid centered on the pDSGC soma. A
222 heatmap of glutamatergic EPSC charge transfer evoked by the small flashing spot was
223 generated and overlaid with the reconstructed dendritic arbors for each pDSGC (**Figure**
224 **3A**).
225
226 RF mapping with small flashing spots also revealed a spatial displacement of
227 glutamatergic EPSC distribution that aligns well with the displacement determined by
228 larger spots presented to the pDSGC periphery (**Figure 3B**). Similar to the
229 displacement pattern revealed by stimulation of the RF periphery, the strongest
230 glutamatergic EPSCs are preferentially located on the preferred side of pDSGC somas
231 (**Figure 3C**). Notably, for most cells, the center of the glutamatergic EPSC RF is
232 displaced from the center of the dendritic field (**Figure S3A and S3B**), indicating
233 additional mechanisms underlying the glutamatergic RF displacement apart from the
234 dendritic arbor distribution.
235
236 We further examined the strength of the glutamatergic input across the pDSGC
237 On dendritic field (**Figure 3D**). We normalized the EPSC charge transfer by the total

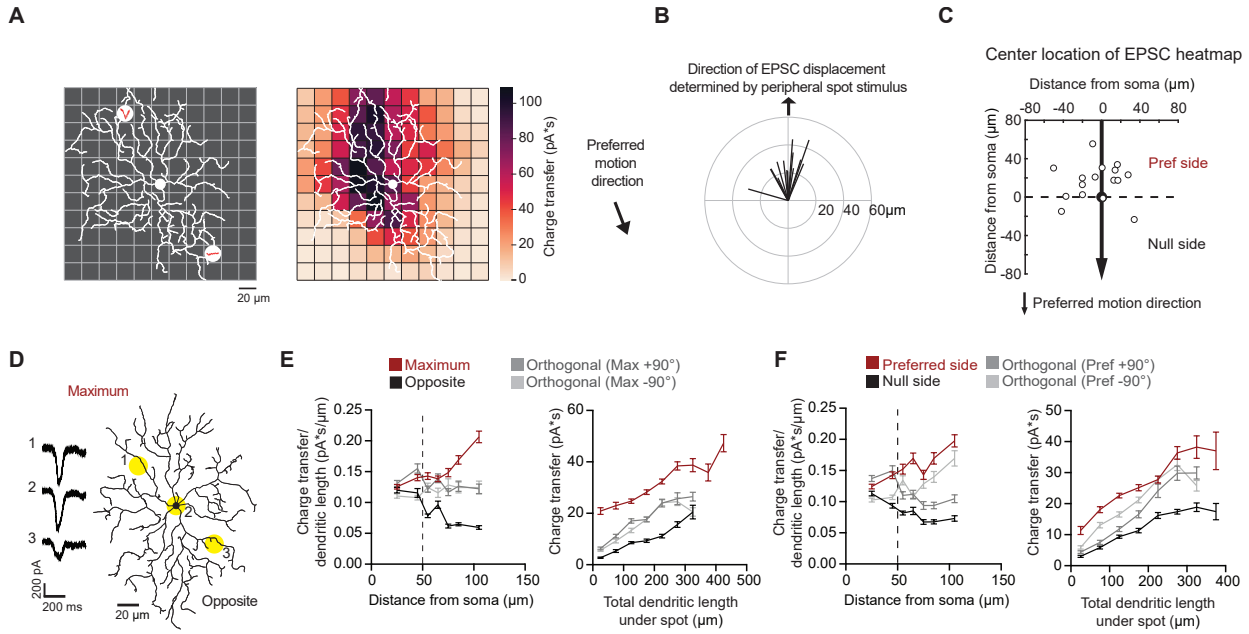

Figure 3. Non-uniform glutamatergic synaptic excitation across pDSGC dendritic span contributes to skewed excitatory receptive field.

(A) Left: Schematic for small spot RF mapping experiment in DHβE + Gabazine. Middle: Example heat map. Right: Preferred motion direction of the example cell. **(B)** Vector sum plot of EPSC charge transfer center of mass determined by small spot RF mapping aligned to the region where a peripheral spot evokes the maximum glutamatergic EPSC (upward arrow). **(C)** Spatial locations showing centers of mass of glutamatergic excitatory charge transfer obtained from experiments illustrated in **A** aligned to each cell's preferred motion direction (15 cells). **(D)** Example EPSC responses to spots presented to a pDSGC along the maximum-opposite axis of glutamatergic RF displacement. **(E)** Left: "EPSC current density" (i.e. ratio of charge transfer per dendritic length) versus distance from soma along the maximum-opposite axis of glutamatergic RF displacement (16 cells, ***$p < 0.001$) as well as the orthogonal regions. Right: Summary plot of glutamatergic charge transfer as a function of total dendritic length centered around the flashing spot for spots shown more than 50 µm away from the soma (16 cells, ***$p < 0.001$). **(F)** Same as **E** but along the preferred-null motion axis (15 cells, charge transfer/dendritic length vs distance from soma **$p = 0.0026$, charge transfer vs dendritic length ***$p < 0.001$). Summary statistics are mean ± SEM.

260 dendritic length in a circle with a 60 μm diameter centered on each small flashing spot.
261 This provides an estimate of the strength of glutamatergic inputs per unit dendritic
262 length, or "EPSC density", at each stimulus location. When we calculated the density
263 along the axis of maximal glutamatergic RF displacement, we found that the EPSC
264 density on the displaced side of the dendritic field is larger than the corresponding
265 region on the opposite side (**Figure 3E**, left). From 50 μm away from the soma, spots on
266 the side corresponding to the maximum displacement (Maximum) yield stronger EPSCs
267 than spots on the opposite side (Opposite), while controlling for the same dendritic
268 length (**Figure 3E,** right). This heterogeneity in EPSC density across the dendritic span
269 persists when comparing EPSC responses along the preferred-direction motion axis of
270 the cell (**Figure 3F**). Analysis of the peak amplitudes showed similar results as charge
271 transfer (**Figures S3C and S3D**).
272
273 Next, we asked what mechanisms could underlie the non-uniform excitatory
274 conductance across the dendritic span. Because bipolar cells provide the dominant
275 excitatory input to DSGCs, the enhanced excitation on the preferred side of the
276 receptive field could stem from increased density or strength of bipolar synapses. Using
277 a published serial block-face scanning electron microscopic (SBEM) dataset of the adult
278 mouse retina (Ding et al., 2016), we reconstructed large numbers of ON starburst
279 amacrine cells and On-OFF DSGCs (**Figures 4A**). The preferred direction of the traced
280 DSGCs was inferred from the mean orientation of starburst dendrites making
281 'wraparound' synapses onto the DSGCs, following the previous work of Briggman et al.
282 (Briggman et al., 2011) (**Figure 4B**). Among all DSGCs, four preferred directions were
283 seen roughly 90 degrees apart, as expected for most retinal locations (Sabbah et al.,
284 2017). We selected three On-Off DSGCs for which the inferred preferred direction of
285 motion fell on the horizontal axis like the cells we studied electrophysiologically, two with
286 one motion preference, and the other with the opposite preference. Technical
287 constraints prevented us from saying which cells preferred posterior motion and which
288 cells preferred anterior motion (see Methods). We then mapped the distribution of
289 bipolar ribbon synapses onto the dendrites of these three cells. We found no marked
290 gradient in ribbon density across the preferred-null motion axis of the three cells
291 (**Figures 4D – 4F, S4A – S4B),** suggesting that the gradient in EPSC density across
292 this axis is not determined by the density of bipolar inputs.
293
294 In addition to ribbon density, we also examined the time course of glutamatergic
295 EPSCs in the presence of DHβE and Gabazine along the axis of maximal glutamatergic
296 RF displacement and along the preferred-null motion axis. We found no significant
297 differences in the latency, rise and decay times in EPSC waveforms across the axis of
298 maximal glutamatergic RF displacement in response to the small flashing spots
299 (**Figures 4G – 4I,** left panels). In addition, we did not detect a monotonic change in
300 glutamatergic EPSC kinetics along the preferred-null motion axis in DHβE and

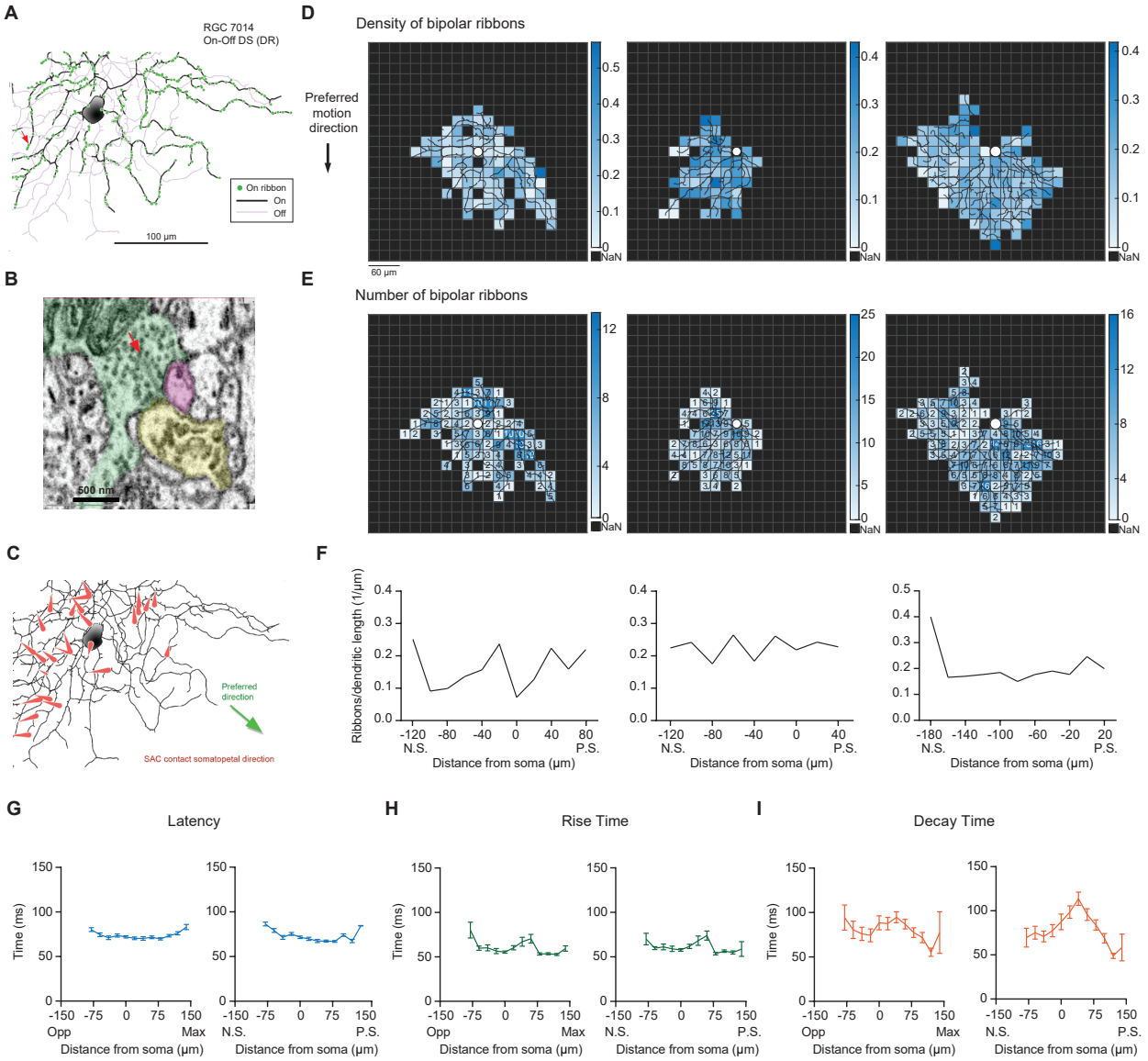

Figure 4. Neither the density of bipolar ribbon inputs nor the kinetics of glutamatergic EPSCs varies systematically along the axis of RF displacement.
(A) Top: Distribution of ribbon synaptic input to one of the three reconstructed On-Off DSGCs. **(B)** Ultrastructure of the synapse indicated by the red arrow in **A**, as visualized by serial block-face electron microscopy. The presynaptic bipolar cell (green) belongs to Type 5t. Red arrow marks the ribbon. The magenta profile belongs to the On-Off DSGC. The other postsynaptic partner at this dyad synapse was another ganglion cell (yellow). Though only a fragment was included in the volume, it was presumably a DSGC, since it costratified entirely with the inner dendrites of the On-Off DSGC (**A**; black dendrites). **(C)** SAC inputs onto example On-Off DSGC. Red arrows indicate the direction and location of the SAC inputs on the DSGC dendrites. **(D)** Density map of bipolar ribbon synapses for 3 example On-Off DSGCs with estimated preferred directions along the posterior-anterior axis (see Methods). The soma location is indicated by the white spot in the center. **(E)** Bipolar ribbon heat map for the 3 example cells, respectively. The number of ribbons in each square are indicated. **(F)** Quantification of ribbon density across the preferred-null axis, respectively. The soma location is at 0. (N.S. = null side, P.S. = preferred side). **(G)** Left: Summary of latency of glutamatergic EPSC responses along the maximum-opposite axis (Max = maximum glutamatergic EPSC region, Opp = opposite region)(16 cells, $p = 0.75$). Right: Summary of latency along the preferred-null motion axis (N.S. = null side, P.S. = preferred side)(16 cells, $p = 0.88$). **(H)** Same as in **G**, except for rise time (10% - 90%). (Left: $p = 0.12$, right: $p = 0.21$, 16 cells). **(I)** Same as in **G**, except for decay time (90% - 30%). (Left: $p = 0.25$, right: $p = 0.26$, 16 cells). Summary statistics are mean ± SEM.

323 Gabazine (**Figures 4G – 4I,** right panels) or in DHβE only (**Figures S4C and S4D**).
324 Similar glutamatergic EPSC waveforms across the pDSGC dendritic field contrast with a
325 previous study of On DSGCs reporting a gradient of EPSC temporal kinetics from
326 slow/sustained to fast/transient corresponding to different bipolar cell subtypes along
327 the preferred-null motion axis to implement a Hassenstein-Reichardt-Detector-like
328 mechanism for their direction selectivity (Matsumoto et al., 2019).
329
330 **Null-direction response emerges during partial activation of the displaced pDSGC**
331 **RF**
332
333 Because On-Off DSGCs are thought to be dedicated to encoding object motion,
334 we next asked how the displaced excitatory RF of the pDSGC revealed by the
335 stationary flashing stimuli contributes to motion processing. We reasoned that because
336 conventional simple motion stimuli such as moving bars and drifting gratings traverse
337 the entire RF of the pDSGC, SAC-mediated inhibition would exert a dominant influence
338 on pDSGC spiking by strongly suppressing the pDSGC null-direction response.
339 However, when motion trajectories are more complex, as often occurs in the natural
340 environment, the displaced excitatory pDSGC RF may confer additional characteristics
341 to the cell's motion encoding. Therefore, we investigated how the direction-selective
342 circuit would process interrupted motion because moving objects in the natural
343 environment often pass behind occluders or start moving after being stationary.
344
345 To examine if the displaced excitatory RF of the pDSGC plays a role in encoding
346 interrupted motion, we created an occluded motion stimulus where a moving bar
347 disappeared behind a central occluder 220 μm in diameter (**Figure 5A**). The occluder
348 covered the dendritic span of the pDSGC and a substantial portion of its RF center. In
349 contrast to the full-field motion stimuli, the occluded motion stimulus caused both
350 preferred and null-direction On spiking responses (**Figures 5B and S5A**). These
351 responses are only evoked when the bar travels in the preferred side, which
352 corresponds to the displaced side of the pDSGC RF (**Figure 5B**, middle row, **5C**). In
353 contrast, no spiking response is evoked when the bar moves across to the null side
354 beyond the occluder (**Figures 5B,** bottom row, **5C**). To test whether this regional
355 difference is due to the asymmetric wiring between SACs and DSGCs, we blocked the
356 cholinergic and GABAergic transmission with DHβE and gabazine and saw that the
357 regional difference persisted (**Figures 5C and S5B**). Consistent with the spiking
358 pattern, the EPSC responses also reflected this regional asymmetry (**Figure 5D**).
359
360 Moreover, we blocked $GABA_C$ receptor activity, glycine receptor activity, and
361 gap-junction coupling with TPMPA, strychnine and MFA, respectively, and found that
362 the spatial asymmetry of the spike response remains during the occluded motion

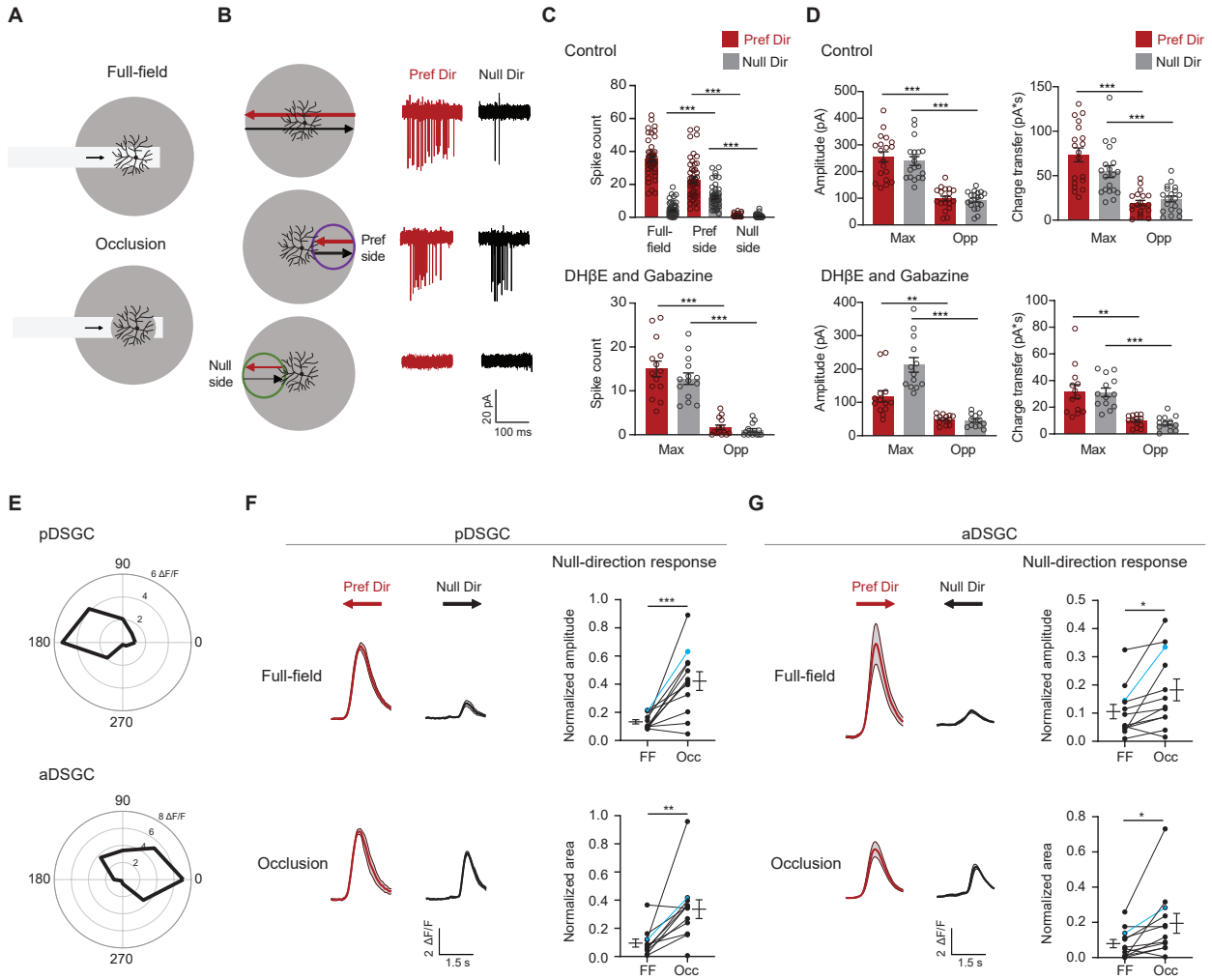

Figure 5. Displaced excitatory receptive field contributes to null-direction responses in the preferred region.

(A) Full-field moving bar and occluded bar stimuli. **(B)** Example On spiking responses of a pDSGC to full-field bar (top) and occluded bar stimulus (middle, bottom) moving in the preferred (red) and null (black) directions. **(C)** Top: Mean spike counts of pDSGCs to the full-field moving bar (full-field) and the occluded moving bar on the preferred side and null side (48 cells). Bottom: Mean spike counts in DHβE + Gabazine to the occluded bar stimulus in the region evoking the maximum spiking (Max) and the opposite region (Opp) (13 cells). **(D)** Mean pDSGC EPSC peak amplitude and charge transfer in the region evoking the maximum response (Max) and the opposite region (Opp) in the control (top, 19 cells) and DHβE + Gabazine (bottom, 13 cells) conditions. (In DHβE + Gabazine: Pref Dir – Max vs Pref Dir – Opp amplitude **p = 0.0028, Pref Dir – Max vs Pref Dir – Opp charge transfer **p = 0.0012). **(E)** Top: Example directional tuning curve of GCaMP6 signal of a pDSGC. Bottom: Example tuning curve of an aDSGC. **(F)** Top left: Example GCaMP6 fluorescence traces of a pDSGC for the full-field moving bar in the preferred (red) and null (black) directions. Bottom left: Example GCaMP6 traces of the cell for the occluded bar stimulus. Top right: Normalized amplitude of the posterior-preferring cell null-direction response during the full-field bar and the occluded bar (12 cells). Bottom right: Normalized area of the null-direction response during the full-field bar and the occluded bar (12 cells, **p = 0.0035). **(G)** same as in **F**, except for aDSGCs. (12 cells, normalized amplitude *p = 0.013, normalized area *p = 0.019). Summary statistics are mean ± SEM, ***p < 0.001 except where specified otherwise.

385 stimulus (**Figures S5C – S5E**). Based on these pharmacology results, we conclude
386 that the asymmetric glutamatergic RF of the pDSGC contributes to robust spiking in
387 both null and preferred directions when the preferred side of the RF is activated by the
388 occluded motion stimulus.
389
390 Since there are two On-Off DSGC subtypes that are tuned to the opposite
391 directions along the posterior-anterior axis, we investigated if the anterior-direction-
392 selective DSGC (aDSGC) exhibits the same null-direction response pattern to the
393 occluded motion stimulus as the pDSGC. To identify both DSGC subtypes, we
394 performed calcium imaging of GCaMP6-expressing RGCs in another transgenic mouse
395 line carrying Vglut2-IRES-Cre and floxed GCaMP6f (**Figure S6A**) during the full-field
396 moving bar stimulus. We then used an online analysis to identify aDSGCs and pDSGCs
397 based on the directional tuning of their calcium signals to the anterior and posterior
398 motion directions (**Figures 5E and S6B – C**). Next, we centered the occluded motion
399 stimulus on individual aDSGC and pDSGC somas and performed calcium imaging
400 during the occluded motion stimulus. Consistent with pDSGC spiking activity, a
401 significant null-direction calcium response of the pDSGCs was evoked when the
402 occluded moving bar traveled across the receptive field to the preferred side of the RF
403 (**Figures 5F and S6D**). Notably, aDSGCs also exhibited a null-direction response to the
404 occluded motion stimulus that is similar to that of pDSGCs (**Figure 5G and S6D**),
405 indicating that aDSGC RFs are also displaced to the preferred side.
406
407 The above results show that continuous motion interrupted by a stationary
408 occluder in the center of the pDSGC's RF causes unexpected null-direction spiking as
409 the bar emerges from behind the occluder into the preferred side of the pDSGC RF.
410 However, this occluded motion stimulus cannot distinguish whether the interruption itself
411 or only the start position of the emerging bar was necessary for the null-direction
412 response. Therefore, we created a stimulus where a growing edge of a moving bar
413 would emerge at different locations along the preferred-null motion axis of the cell
414 (**Figure 6A**). For the null-direction moving bar, there is an increase in both the spike
415 number and the firing rate as the starting position of the moving bar is located past the
416 soma on the preferred side of the pDSGC RF (**Figures 6A – 6C**). Thus, the emergent
417 growing edge caused null-direction spiking of pDSGCs in a similar pattern as the
418 moving bar emerging behind the central occluder. These results illustrate that the null-
419 direction response of the pDSGC during the occluded motion stimulus is dependent on
420 the position in the receptive field from which the moving edge emerges, not the previous
421 motion approaching the occluder.
422
423

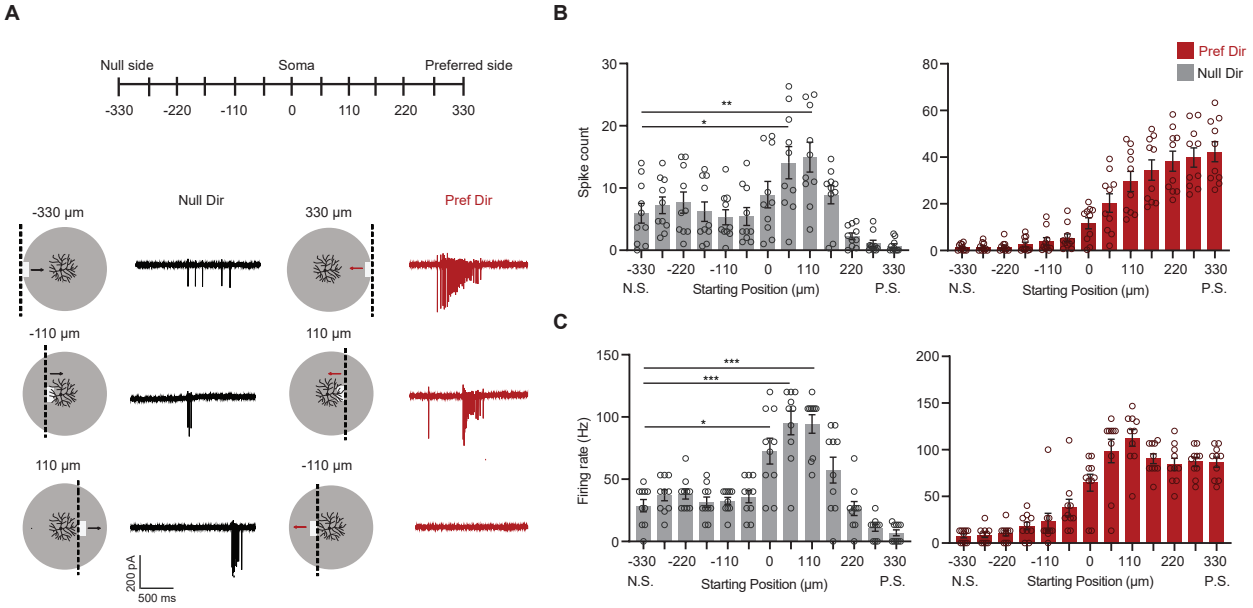

Figure 6. Null-direction response is dependent on start position of emerging bar. **(A)** Schematic of moving bars emerging from different locations along the DSGC's preferred-null motion axis and example spiking responses. The soma location is at 0. Vertical dashed lines on the schematic indicate the positions of the emerging leading edge of the moving bar. **(B)** Mean spike counts (null direction: -330 vs 55 *p = 0.012, -330 vs 110 **p = 0.0088) and **(C)** firing rates (null direction: -330 vs 0 *p = 0.014) to bars emerging from different locations along the preferred-null motion axis (10 cells). Summary statistics are mean ± SEM, ***p < 0.001 except where specified otherwise.

435 **Null-direction responses of DSGCs during partial activation of their RFs can be**
436 **useful for decoding object location**
437
438 Because of their displaced RFs, pDSGCs generate robust spiking activity in both
439 the preferred and null directions when a moving object appears and starts moving on
440 the preferred side of the cell's RF, as when an object emerges from behind an occluder
441 positioned over the cell's soma. We asked whether this prima facie aberrant signaling
442 can have a functional role relevant to the behavioral goals of the organism. We
443 hypothesize that partial RF activation of a DSGC at a given region in visual space may
444 provide precise information about the spatial position of a moving object along an
445 interrupted motion trajectory. In particular, if a moving object emerging from behind an
446 occluder activates the preferred side of an On-Off DSGC's RF, this DSGC would
447 generate a null-direction spiking response together with the preferred-direction
448 response of a nearby On-Off DSGC subtype preferring the opposite motion direction
449 (**Figure 7A**). Such synchronous spiking activity between DSGCs of opposite preferred
450 directions at the location of the occluder could yield a stronger and more localized
451 spatial signal at the population level in response to interrupted motion.
452
453 To test how the null-direction response during interrupted motion might enhance
454 downstream estimation of stimulus position, we simulated the spiking responses of
455 pDSGCs in a one-dimensional model consisting of On-Off DSGC subtypes that prefer
456 opposite motion directions on the posterior-anterior axis (aDSGCs and pDSGCs, **Figure**
457 **7A**). One hundred cells of each subtype were arranged along the preferred motion axis
458 of both groups such that the spatial positions of the two subtypes were uncorrelated.
459 We simulated a bright edge moving along this axis in a single direction at a constant
460 velocity under both uninterrupted and interrupted motion conditions and analyzed the
461 On response to the edge. The mean spiking response of each DSGC was modeled as a
462 rectified sine wave with parameters obtained from our experimental data (**Figures 7B –**
463 **7D** and **S7**), and sub-Poisson trial-to-trial variability was introduced to the mean spiking
464 response on each trial (**Figure S7D**). The spatial positions of the DSGCs were shuffled
465 in each simulation block to allow us to average over different spatial arrangements of
466 the RFs.
467
468 Using a population vector decoder (see Methods), we compared the scenario in
469 which none of the DSGCs were occluded (full-field) with the scenario in which a single
470 occluder was placed over a DSGC that prefers the direction opposite to the motion
471 direction of the moving edge (occlusion). The occluded DSGC's spiking response to an
472 edge moving in its null direction certainly degrades direction estimation and appears to
473 be a defect of the direction-selective circuit. Nevertheless, the coincidence of this null-
474 direction response from a pDSGC and the preferred-direction responses of neighbor

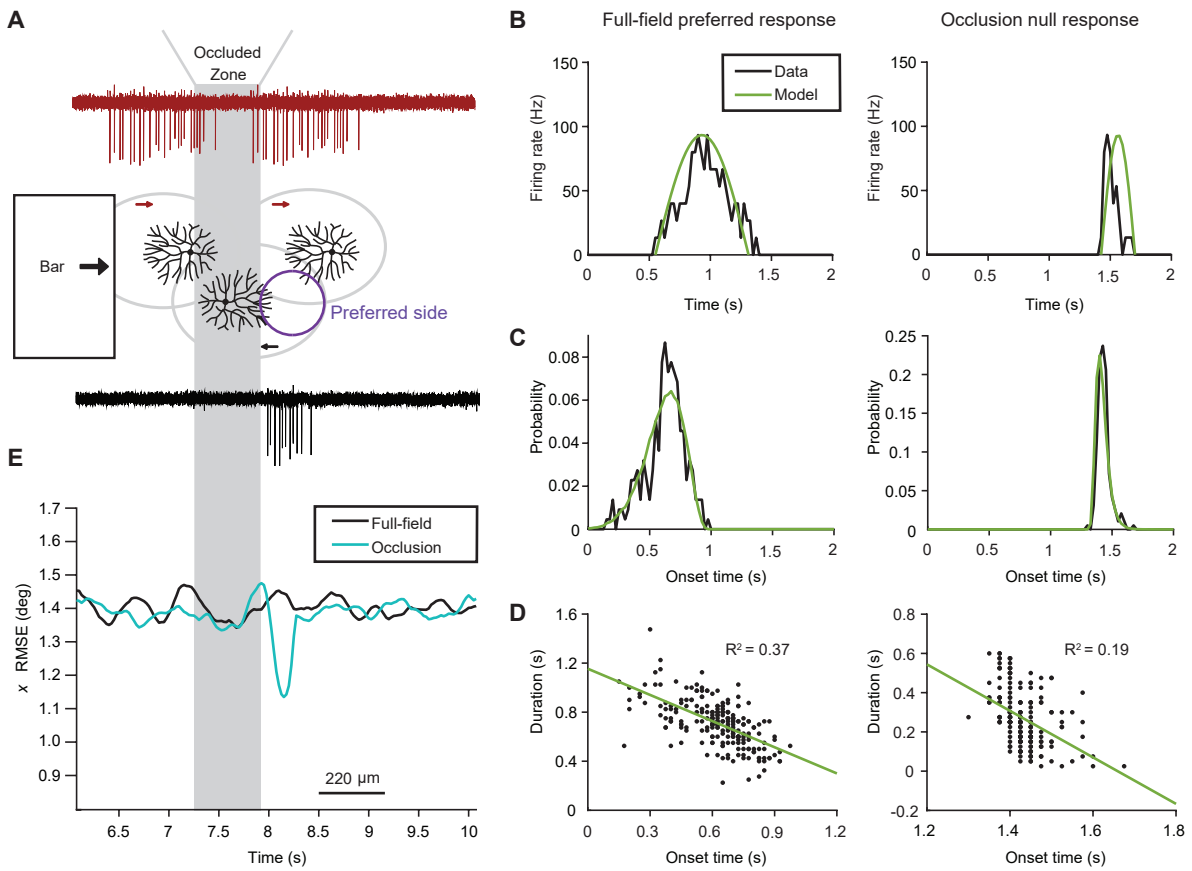

Figure 7. Null-direction spiking of On-Off DSGCs during the occluded motion stimulus improves position estimation.

(A) Schematic of one-dimensional DSGC population model along with example spike trains for two pDSGCs (red trace showing their preferred-direction responses) and an a DSGC (black trace showing its null-direction response). An occluder 220 µm wide (shaded bar) was centered on the soma of the aDSGC. **(B)** Example half sine wave fits (green) to PSTHs obtained from experimental data (left: full-field, 73 cells; right: occlusion, 69 cells). **(C)** Fits to probability distributions of spike response onset times (left: full-field, 73 cells; right: occlusion, 69 cells). **(D)** Linear correlation between spike response duration and spike response onset time (left: full-field, 73 cells; right: occlusion, 69 cells). **(E)** Root-mean-square error in estimating the position of the light bar's leading edge for full-field (black) and occluded (blue) motion.

aDSGCs that prefer motion in the anterior direction reduces the error in the population estimate of the edge's spatial position by ~15 percent (**Figure 7E**). The synchronous firing may, itself, also be a useful alarm signal to trigger attention downstream of the retina, independent of the precise position information it might additionally convey. In conjunction with other retinal cell types in the mouse that encode the location of moving objects, On-Off DSGCs may contribute to fine spatial discrimination during interrupted motion in complex natural scenes.

Discussion

Our study reveals a new form of asymmetry in the direction-selective circuit: a spatial displacement of glutamatergic inputs to the preferred side of the On-Off pDSGCs due to a non-uniform distribution of synaptic conductances across the pDSGC dendritic span. The impact of this displaced excitation on DSGC spiking is demonstrated by using moving stimuli with interrupted trajectories, a feature abundant in natural scenes. In contrast to full-field continuous motion which maximizes the contribution of SAC-mediated null-direction inhibition, occluded motion stimuli reduce the contribution of SAC-mediated inputs to allow the excitatory receptive field to dominate the spiking response in a non-directional manner when only part of the RF is stimulated. Therefore, an On-Off DSGC's response is dynamically shaped by visual stimulus-dependent interactions of excitatory and inhibitory synaptic circuitries and may flexibly represent motion direction or motion location in a context-dependent manner.

The non-isotropic excitation of the pDSGC alludes to a more sophisticated set of wiring and signaling mechanisms from the bipolar cell population (Franke et al., 2017). A detailed explanation of the glutamatergic RF displacement awaits future studies. The gradient of glutamatergic current density across the pDSGC dendritic span may arise from a number of possible scenarios including varying strengths of individual glutamatergic synapses, heterogeneous membrane properties across pDSGC dendritic field, and contribution from Vglut3+ amacrine cells (Kim et al., 2015; Lee et al., 2016). Although our study focuses on the On component of the direction-selective circuit, we observed a similar pattern of RF displacement for the pDSGC Off response, suggesting similar mechanisms operating in the Off layer of the IPL.

We combined experimental recordings and theoretical analysis to obtain insights into the nature of the visual information encoded by On-Off DSGCs during interrupted motion. Previous theoretical analysis has addressed the encoding of motion direction by DSGCs at the population level (Fiscella et al., 2015; Kühn and Gollisch, 2019; Zylberberg et al., 2016). In this study, we explored a new hypothesis that On-Off DSGC population activity contains information about both the direction and the location of a

530 moving object. When a moving object emerges from an occluder, the null-direction
531 response of an On-Off DSGC is synchronized with the preferred-direction responses of
532 On-Off DSGCs preferring the opposite direction with overlapping spatial RFs. Since
533 synchronized activity among RGCs has been shown in multiple species to encode
534 ethologically relevant visual information (Ishikane et al., 2005; Schwartz et al., 2007), it
535 is possible that the highly localized and synchronized firing of oppositely tuned DSGC
536 types may render the object emerging from behind the occluder more salient by
537 enhancing positional information. For instance, when a predator moves suddenly from
538 behind an occluding object, a mouse may prioritize information about the predator's
539 position over its direction of movement. The encoding of both motion direction and
540 spatial location may be particularly useful in the superior colliculus (SC) where On-Off
541 DSGC inputs are targeted to the superficial layer (Huberman et al., 2009; Shi et al.,
542 2017), as the colliculus supports threat evaluation and visually guided eye and head
543 movements (Ito and Feldheim, 2018).
544
545 It is likely that other ganglion cell types, such as W3-RGCs and HD-RGCs (Kim
546 et al., 2010; Zhang et al., 2012; Jacoby and Schwartz, 2017), also participate in fine
547 spatial discrimination and motion encoding. However, because no other ganglion cell
548 types are known to project to the same regions of the dorsal lateral geniculate nucleus
549 (dLGN) and the SC as On-Off DSGCs (Huberman et al., 2009; Kay et al., 2011; Sanes
550 and Masland, 2015; Shi et al., 2017), they may not participate in the same visual
551 processing tasks as On-Off DSGCs or may provide complementary information about
552 spatial location of moving objects. The synchronous firing of two typically asynchronous
553 On-Off DSGC subtypes may, in and of itself, form a useful attention signal downstream
554 of the retina. Elucidating the roles of diverse RGC types in motion encoding requires a
555 thorough understanding of visual signal transforms along pathways and how the visual
556 system instructs visually guided behavior.
557
558 Together, our study demonstrates how a visual neuron's response is determined
559 by stimulus-dependent assembly of circuit components, and thereby provides insights
560 into the neural basis of context-dependent visual encoding of complex natural
561 environments.
562
563
564
565
566
567
568
569
570
571

572 **Acknowledgements**
573 We thank Chen Zhang for managing the mouse colony and Dr. John Maunsell, Dr.
574 Siwei Wang, Mathew Summers, Malak El-Quessny, and Benjamin Hoshal for advice on
575 the manuscript. This work was supported by NIH R01 EY02416 and the McKnight
576 Scholarship Award to W. W., the NSF GRFP DGE-1746045 to J.D., NIH F31 EY029156
577 to H.E.A., the NSF Career Award 1652617 and the Physics of Biological Function PHY-
578 1734030 to S.E.P., and NIH RO1 EY012793 to D.B.
579
580 **Competing Interests**
581 All authors would like to report no competing interests.
582
583 **Methods**
584
585 **Animals**
586 *Chat-IRES-Cre* mice (129S6-Chat$^{tm2(cre)Lowl}$/J) and floxed *tdTomato* mice (129S6-
587 *Gt(ROSA)26Sor*$^{tm9(CAG\text{-}tdTomato)Hze}$/J) were acquired from the Jackson Laboratory. *Drd4-*
588 *GFP* mice were originally developed by MMRRC
589 (http://www.mmrrc.org/strains/231/0231.html) and were backcrossed to the C57BL/6
590 background. These lines were crossed so that both pDSGCs and SACs were labeled.
591 *Vglut2-IRES-Cre* mice and floxed *Ai95(RCL-GCaMP6f)-D* mice were acquired from
592 Jackson Laboratory and were crossed and used for calcium imaging experiments. Mice
593 of ages P21 – P60 of either sex were used. All procedures regarding the use of mice
594 were in accordance with the University of Chicago Institutional Animal Care and Use
595 Committee and with the NIH Guide for the Care and Use of Laboratory Animals and the
596 Public Health Service Policy.
597
598 **Whole-mount retina preparation**
599 Mice were dark adapted for 1 hour and then were anesthetized with isoflurane and
600 euthanized by decapitation. Retinas were isolated at room temperature in oxygenated
601 Ames' medium (Sigma-Aldrich, St. Louis, MO) under infrared illumination. The retinas
602 were separated into dorsal and ventral halves and were mounted ganglion-cell-layer up
603 on top of a ~1.5 mm^2 hole in a small piece of filter paper (Millipore, Billerica, MA). The
604 orientation of the posterior, anterior, inferior, and superior directions were noted for each
605 piece. During the experimental day, the mounted retinas were kept in darkness at room
606 temperature in Ames' medium bubbled with 95% O_2/ 5% CO_2 until use (0 – 8h).
607
608 **Visual stimulation**
609 A white organic light-emitting display (OLEDXL, eMagin, Bellevue, WA; 800 X 600 pixel
610 resolution, 60 Hz refresh rate) was controlled by an Intel Core Duo computer with a
611 Windows 7 operating system and was presented to the retina at a resolution of 1.1

612 μm/pixel. Visual stimuli were generated using MATLAB and the Psychophysics Toolbox,
613 and were projected through the condenser lens of the two-photon microscope focused
614 on the photoreceptor layer.
615
616 For the peripheral spot experiments, stationary spots of size 110 μm diameter were
617 presented 165 μm away from the soma of the recorded pDGSC for 2 seconds. At this
618 distance, these spots were presented outside of the dendritic span of the majority of
619 recorded pDSGCs. These spots were presented in 8 different locations
620 pseudorandomized around the recorded pDSGC, with 3 repetitions each.
621
622 For moving bar experiments, a bright moving bar with dimensions 110 μm (width) X 880
623 μm (length) and speed 330 μm/s moved in 8 different pseudorandomized directions
624 across the receptive field of the pDSGC, with 3 – 6 repetitions each. The occluded bar
625 stimulus was the same as the moving bar stimulus except for the addition of a central
626 occluder with a diameter size of 220 μm which obscured the movement of the bar. The
627 size of the occluder was large enough to obscure the entire dendritic span for the
628 majority of recorded pDSGCs.
629
630 For the emergent moving bar experiments where the bar emerged from different
631 locations of the receptive field, a bright moving bar with dimensions 110 μm (width) X
632 440 μm (length) and speed 330 μm/s could start moving pseudorandomly from 13
633 different locations across the receptive field (Figure 5). The bar could move in the
634 preferred or null direction of the recorded cell.
635
636 For the receptive field mapping experiments, bright spots with a 20 μm diameter were
637 presented across the receptive field of the recorded pDSGC. They were shown for 3 – 4
638 repetitions with a duration of 400 ms in a random sequence within an 11 X 11 grid,
639 covering a total area of 220 X 220 μm^2. To examine the kinetics of EPSCs, bright spots
640 with either a 20 μm diameter (for DHβE and gabazine experiments) or a 60 μm diameter
641 (for DHβE experiments) were shown across the receptive field in a random sequence
642 within an 11 X 11 grid for 3 – 4 repetitions. Spots were shown with a duration of 400 ms.
643
644 The light intensity for bright peripheral spot experiments, the moving bar and occlusion
645 experiments, and the receptive field mapping experiments was ~1.6×10^4 R*/rod/s.
646
647 **Targeting cells for electrophysiology**
648 Cells were visualized with infrared light (>900 nm) and an IR-sensitive video camera
649 (Watec). DSGCs were targeted with the aid of two-photon microscopy in *Drd4-GFP*
650 mice. Cell identity was confirmed physiologically by extracellular recordings of
651 responses to moving bars and/or by filling the cell with 25 μM Alexa 594 (Life

652 Technologies) to show bistratified dendritic morphology. Because the tissue was aligned
653 on the filter paper, we confirmed that the preferred direction of the spiking responses to
654 moving bar aligned well with the anatomical posterior (visual field coordinate) or nasal
655 (retinal coordinate) direction.
656
657 **Quantification of dendritic morphology**
658 The ON layer of each cell was isolated from a z-stacked image in ImageJ. To calculate
659 the radius, a contour of the dendritic span was made by drawing a boundary around the
660 dendritic tips, and the area within the contour and resulting equivalent radius was
661 calculated. For calculating dendritic length, the On layer from the z-stack projection was
662 traced in NeuronStudio. The two-dimensional trace was then exported to MATLAB.
663 Dendritic length was calculated in MATLAB using a custom-written code. We subdivided
664 the cell into eight sectors for analysis. Sectors extended out from the soma and were
665 aligned to the spot stimulus such that each spot was at the center between each
666 sector's radial boundaries. When computing normalized vector sums (Figures 2B – C,
667 S2A – S2B), total dendritic length in each sector was normalized by the total dendritic
668 length of the cell.
669
670 **Serial electron-microscopic analysis**
671 We reconstructed DSGCs and starburst amacrine cells from a previously published
672 SBEM dataset (Ding et al., 2016). These cell types were easily recognizable from their
673 characteristic dendritic arbors and patterns of stratification. We inferred the preferred
674 direction of motion of the DSGCs, relative to the boundaries of the volume from the
675 orientation of SAC dendritic inputs onto the DSGC dendrites, as in Briggman et al.
676 (2011). SAC dendrites preferentially form GABAergic synapses with DSGCs if their
677 orientation, from soma to dendritic tip, corresponds to the null direction of the DSGC.
678 Neither the eye of origin nor the retinal location of the sample was recorded when this
679 sample was acquired, but it was possible to infer the ventral direction within the volume
680 from reconstructions of multiple members of several other RGC types with strong
681 dendritic asymmetries along the dorsoventral axis, including Jam-B RGCs (Kay et al.,
682 2011) and F-RGCs (Rousso et al., 2016). One of the four On-Off DSGC types had an
683 inferred preference for the ventral direction. Thus, we infer that the two types with
684 preferred directions 90 degrees away from this ventral-motion-preferring DSGC type
685 must therefore have been tuned to the horizontal motion axis. We could think of no way
686 to distinguish which of these types prefers anterior motion and which prefers posterior
687 motion.
688
689 Ribbon synapses from On bipolar cells onto the dendrites of these three DSGCs were
690 mapped manually. The branching patterns of all cells were reconstructed using

691 skeletons and synapses were marked with single nodes using the Knossos software
692 package (https://knossostool.org/).
693
694 To measure local ribbon density across the DSGC dendritic field, the dendritic span was
695 divided into individual squares with 10 x 10 µm (Figure S4) or 20 x 20 µm (Figure 4)
696 dimensions. Total dendritic length in each square was calculated in Matlab with a
697 custom-written code. The total number of ribbon synapses in each square was also
698 quantified. Ribbon density was calculated by dividing the ribbon synapse number by the
699 total dendritic length in the appropriate squares.
700
701 **Electrophysiology recordings**
702 Recording electrodes of 3 – 5 MΩ were filled with a cesium-based internal solution
703 containing 110 mM CsMeSO4, 2.8 mM NaCl, 4 mM EGTA, 5 mM TEA-Cl, 4 mM
704 adenosine 5′-triphosphate (magnesium salt), 0.3 mM guanosine 5′-triphosphate
705 (trisodium salt), 20 mM HEPES, 10 mM phosphocreatine (disodium salt), 5 mM N-
706 Ethyllidocaine chloride (QX314),filled with a cesium-based internal solution containing
707 110 mM CsMeSO4, 2.8 mM NaCl, 4 mM EGTA, 5 mM TEA-Cl, 4 mM adenosine 5′-
708 triphosphate (magnesium salt), 0.3 mM guanosine 5′-triphosphate (trisodium salt), 20
709 mM HEPES, 10 mM phosphocreatine (disodium salt), 5 mM N-Ethyllidocaine chloride
710 (QX314), and 0.025 mM Alexa 594, pH 7.25. Retinas were kept in oxygenated Ames'
711 medium with a bath temperature of 32 – 34 °C.
712
713 Data were acquired using PCLAMP 10 and a Multiclamp 700B amplifier (Molecular
714 Devices, Sunnyvale, CA), low-pass filtered at 4 kHz and digitized at 10 kHz. Light
715 evoked EPSCs were isolated by holding cells at -60 mV after correction for the liquid
716 junction potential (~10 mV).
717
718 To isolate the contribution of synaptic inputs, a host of pharmacological agents were
719 perfused in the bath during electrophysiology recordings. 8 µM Dihydro-b-erythroidine
720 hydrobromide (DHβE; from Tocris, Cat#2349); 10 µM SR 9551 hydrobromide
721 (gabazine; from Tocris, Cat #1262); 100 µM Meclofenamic acid sodium salt (MFA; from
722 Sigma-Aldrich. Cat#M4531); 1 µM Strychnine (from Sigma-Aldrich, Cat#S0532); 50 µM
723 TPMPA (from Tocris, Cat#1040).
724
725 **Data analysis of electrophysiological recordings**
726 Spiking data from loose-patch recordings were analyzed using custom protocols in
727 MATLAB. The number of spikes evoked by the On response to the peripheral spots
728 were quantified in MATLAB and averaged across 3 repetitions in 8 spatial locations.
729 Light-evoked EPSC responses to peripheral spots were obtained as well, and 3
730 repetitions of EPSC traces were averaged to obtain the mean peak amplitude and

charge transfer response to each condition. The RSI is determined by (Max - Opp)/(Max + Opp) where Max is the number of spikes, peak amplitude or charge transfer in the region of maximal activation using the peripheral spot stimulus, and Opp is the response in the region directly opposite to the Max region.

For the receptive field mapping experiments, the light-evoked EPSCs in response to spots sized 20 μm in diameter were obtained and averaged across 3 – 4 repetitions. The center of mass of the receptive field was determined using the EPSC charge transfer or amplitude at each square in the 11 X 11 grid. The dendritic length was calculated at each point on the RF stimulus grid by summing the dendritic length in a circle 60 μm in diameter centered on the square of interest. For maximum vs. opposite region analysis and the preferred side vs null side analysis (Figures 3E and 3F), we considered the EPSCs in two 5 X 5 subsets of the total grid located opposite of each other. The preferred-null side of each cell was determined by spiking responses to the full-field moving bar, and the maximum-opposite axis was determined by EPSC charge transfer responses to the peripheral spot experiment performed in DHβE and gabazine. The distance from soma at each grid location was defined as the distance between the center of the square and the soma center.

To estimate the spatiotemporal profile across the maximum-opposite or the preferred-null axis for cells in DHβE and gabazine, the light-evoked EPSCs in response to small spots sized 20 μm in diameter were obtained and averaged across 3 – 4 repetitions (Figures 4F – 4H). To estimate the spatiotemporal profile across the preferred-null axis for cells in DHβE only, the light-evoked EPSCs in response to small spots sized 60 μm in diameter were obtained and averaged across 3 repetitions (Figures S4C –D). For both experiments, EPSC parameters of latency, rise time (10 - 90%), and decay time (90 - 30%) were quantified. The preferred-null axis of each cell was determined by spiking responses to the full-field moving bar, and the maximum-opposite axis was determined by EPSC charge transfer responses to the peripheral spot experiment performed in DHβE and gabazine. The parameters of latency, rise time, and decay time were averaged across the squares at equal distances along the cell's preferred-null axis or maximum-opposite axis.

Spiking data evoked by the On and Off responses to the moving bar and occlusion stimuli were quantified in MATLAB using 3 – 6 repetitions in 8 different directions. Spiking data evoked by the bar starting in different positions were quantified in MATLAB across 3 repetitions in the preferred and null directions.

771 **Calcium imaging in posterior- and anterior-preferring On-Off DSGCs**
772 Genetically encoded calcium indicator GCaMP6f was expressed in all RGCs by
773 crossing *Vglut2-IRES-Cre* mice (JAX 016963-*Slc17a6*$^{tm2(cre)Lowl}$) and floxed *Ai95(RCL-*
774 *GCaMP6f)-D* mice (JAX 028865-*Gt(ROSA)26Sor*$^{tm95.1(CAG-GCaMP6f)Hze}$/J). GCaMP6f
775 fluorescence from isolated retinas was imaged in a customized two-photon laser
776 scanning fluorescence microscope (Bruker Nano Surfaces Division). GCaMP6 was
777 excited by a Ti:sapphire laser (Coherent, Chameleon Ultra II, Santa Clara, CA) tuned to
778 920 nm, and the laser power was adjusted to avoid saturation of the fluorescent signal.
779 Onset of laser scanning induces a transient response in RGCs that adapts to the
780 baseline in ~3 s. Therefore, to ensure the complete adaptation of this laser-induced
781 response and a stable baseline, visual stimuli were given after 10 s of continuous laser
782 scanning. To separate the visual stimulus from GCaMP6 fluorescence, a band-pass
783 filter (Semrock, Rochester, MA) was placed on the OLED to pass blue light peaked at
784 470 nm, while two notched filters (Bruker Nano Surfaces Division) were placed before
785 the photomultiplier tubes to block light of the same wavelength. The objective was a
786 water immersion objective (60x, Olympus LUMPlanFl/IR). Time series of fluorescence
787 were collected at 15–30 Hz.

788 We performed an initial direction selectivity test to identify posterior- and anterior-
789 preferring On-Off DSGCs. We recorded GCaMP6f fluorescence from RGC somas within
790 a 75-μm X 75-μm field of view while presenting a full-field moving bar visual stimulus (a
791 bright moving bar 110 μm (width) X 880 μm (length) moving at 330 μm/s across a 660
792 μm circular mask diameter along 8 different directions). At the onset of each moving bar
793 sweep, a TTL pulse was triggered by the visual stimulus computer and recorded by the
794 imaging software to correlate GCaMP6f signals with the direction of each moving bar.
795 Immediately following acquisition of each time series stack, custom-written MATLAB
796 scripts were used to extract fluorescence over time data from time-series images and
797 sort calcium transient by direction of the moving bar. For each RGC soma, raw
798 GCaMP6f fluorescence traces and tuning curves were plotted. On-Off DSGCs were
799 identified by their characteristic singular-lobe directional tuning curves, DSI values ≥ 0.3,
800 and two fluorescence peaks time-locked to the leading (On) and trailing edge (Off) of
801 the moving bar. On-Off DSGCs with preferred directions along the posterior-anterior
802 axis were then selected for further imaging.

803 Once an On-Off DSGC of interest was identified, the visual stimulus was centered to the
804 soma of that cell and a new field of view was drawn to enclose this cell and some
805 background with no GCaMP6f fluorescence. Full-field and occlusion moving bar visual
806 stimulus were presented to the cells as described above (8 directions, 3-4 repetitions).
807 Time series data was collected and subjected to offline analysis.

808

809 **Imaging analysis for calcium imaging**
810 Analysis was performed using ImageJ and MATLAB. Regions of interest (ROIs)
811 corresponding to DSGC soma and background were manually selected in ImageJ. The
812 fluorescent time course of each ROI was determined by averaging all pixels within the
813 ROI for each frame. The fluorescence of the background region was subtracted from
814 the raw fluorescent signal of the soma ROIs at each time frame. The visual stimulus
815 included a 3 – 4 second intersweep interval between the end of one sweep and the start
816 of another. Fluorescence intensities during these intersweep intervals were used to
817 create a baseline (F0) trace for each ROI by fitting either a single- or two-term
818 exponential decay function. Fluorescence measurements were then converted to ΔF/F0
819 values by calculating $\Delta F=(F-F0)/F0$ for every datapoint. The transformed traces were
820 then smoothed using an average sliding window of 4 datapoints. ΔF/F0 traces were
821 clipped, sorted by visual stimulus direction (0, 45, 90, 135, 180, 225, 270, and 315
822 degrees), and averaged over 3-4 trials. Prior to further analysis, ROIs were subjected
823 to a response quality test $QI = Var[Avg.\ Resp]/Avg(Var[R(t)]) \geq 0.45$ to ensure
824 consistency across trials. Responses to the full-field and occlusion moving bars were
825 broken up into On and Off components according to the circular mask entrance and exit
826 times of the leading and trailing edge, respectively. Peak, area ΔF/F0, and time of peak
827 values were calculated for On, Off, and the full trace along all 8 directions. Direction
828 selectivity index (DSI), vector sum, and preferred direction were calculated for both On
829 and Off components.
830
831 **Statistical analysis**
832 Grouped data are presented as mean ± SEM. The Kolmogorov-Smirnov test was used
833 to test data for normality. Student's t-test was used for statistical comparisons of paired
834 samples in Figures 1 and 2. One-way analysis of variance was performed on grouped
835 data in Figures 5 and 6 and subjected to Bonferroni correction.
836
837 For the EPSC/dendritic length vs distance from soma experiments, we performed linear
838 regression analysis using an additional categorical predictor variable indicating the
839 maximum-opposite or the preferred-null side. The p-value associated with interaction
840 term (distance*region) in the resulting model was used to determine whether the slopes
841 are significantly different between the two regions. For the EPSC vs dendritic length
842 experiments, we again performed linear regression with an additional categorical
843 predictor variable indicating the maximum-opposite or preferred-null region. The p-value
844 associated with the categorical predictor in the resulting model was used to determine
845 whether the y-intercepts were significantly different between the two regions. The p-
846 value associated with the categorical predictor was used to determine whether the y-
847 intercepts were significantly different between regions. The number of branches in each
848 square of the grid was determined by a custom MATLAB code.

For the kinetic analyses of EPSC parameters of latency, rise time, and decay time, we performed linear regression analysis to determine whether a statistically significant linear relationship exists between the distance from the soma and each EPSC parameter.

For all data sets, $p < 0.05$ was considered significant. *$p < 0.05$; **$p < 0.01$; ***$p < 0.001$.

Experimental parameters for population model

Experimental data for the spiking response to full-field (73 cells) and occlusion (69 cells) stimuli were obtained. 3 – 6 repetitions were obtained for each full-field or occlusion protocol. The baseline firing rate for each repetition was obtained by binning the spiking response in 25-ms time bins and taking the maximum firing rate during a silent period where no stimulus was displayed, and the baseline firing rate was averaged across all repetitions.

To model the spiking response of the pDSGCs, we binned the spikes evoked by the On response to the motion stimulus in 25-ms time bins and plotted the PSTHs for all 8 motion directions. Then, we fit a rectified sine wave to the PSTH of each pDSGC. We defined the threshold for above-baseline firing to be 4 SD above the baseline firing rate. The onset of the spiking response was determined by the time bin at which the firing rate exceeded the threshold and was immediately followed by a second above-threshold bin (Rate change method; Levakova et al., 2015). We inspected the spiking response onset times returned by our detection algorithm and manually adjusted the spiking response onset times for 3 out of 91 pDSGCs to match the experimental data.

Onset times of spiking responses to the full-field bar moving in the preferred direction ± 45 degrees were similar to those of the preferred-direction response (Figure S7A, left). Likewise, onset times of spiking responses to the occlusion stimulus moving in the null direction ± 45 degrees were similar to those of the null-direction response (Figure S7A, right). Therefore, we included onset times of spiking responses to motions in the directions ± 45 degrees from the preferred-null motion axis in our analysis. Four-parameter beta distributions were fit to histograms of spiking response onset times for preferred- and null-direction motions (Figure 7C). The four parameters included two shape parameters and two parameters that specify the minimum and maximum of the distribution's range.

To determine the offset of the spiking response, we used the algorithm for identifying spiking response onset. Unlike the protocol for determining spiking response onset, however, the detection algorithm started from the most recent time bin and traversed

backwards in time. The offset of the spiking response was defined to be the time bin at which the firing rate exceeded the threshold in two out of three consecutive time bins. For each pDSGC, we calculated the spiking response duration by finding the difference between the spiking response onset and offset times. Furthermore, we calculated the linear correlation between spiking response duration and onset (Figure 7D). Figure S7B shows that using only spiking responses to motion along the preferred-null motion axis and using spiking responses to motion along the preferred-null motion axis as well as motion in the directions 45 degrees away from the preferred-null motion axis yielded consistent results. We also calculated the linear correlation between peak firing rate and spiking response onset, but the correlation was not significant for the full-field protocol (Figure S7C).

Motion direction tuning curves

We computed motion direction tuning curves for all pDSGCs exposed to the full-field moving bar stimulus (73 cells) using the CircStat toolbox in MATLAB developed by P. Berens (2009). The height of each tuning curve was given by the total spike count evoked during the presentation of the full-field moving bar stimulus. We fit a Gaussian function to the histogram of the tuning curve widths (Figure S7E). Figure S7F shows all the normalized motion direction tuning curves. The heights of the tuning curves were rescaled by dividing by their peaks and the widths of the tuning curves were rescaled by dividing by their angular deviation, which is the square-root of twice the circular variance. The normalized tuning curves were fit to a one-term Gaussian model (Figure S7F).

One-dimensional population model

In our computational model, we arranged two populations (left motion-preferring and right motion-preferring) of DSGCs in a horizontal one-dimensional array. Each population had 100 cells, and the nearest neighbor distance distribution within each population was Gaussian, with a mean of 39 μm and a SD of 16 μm (Huberman et al., 2009). The spatial positions of the DSGCs between the two populations were uncorrelated.

Each DSGC's mean spiking response to the moving edge was modeled as a rectified sine wave. The amplitude of the sine wave was given by the peak firing rate, while the period and phase were determined by the spiking response duration and onset time, respectively. For each spatial arrangement of DSGCs, we sampled peak firing rates directly from our experimental data. We sampled spiking response onset times from our four-parameter beta distributions (Figure 7C) and determined the spiking response durations by finding the linear correlation between the two (Figure 7D).

Noise was introduced into the preferred directions of the DSGCs so that they were not all perfectly aligned with the left/right motion axis. To determine the degree of jitter in a DSGC's preferred direction, we sampled from a uniform distribution ranging from -14.1 degrees to +14.1 degrees, where 0 degrees represented a preference for motion directly along the left/right motion axis (Fiscella et al., 2015).

To determine the motion direction tuning width of each simulated DSGC, we sampled circular variances from a Gaussian distribution fit to the histogram of circular variance of the tuning curves from our experimental data (Figure S7E). We scaled the collapsed tuning curve (Figure S7E) by the sampled tuning width and peak firing rate to obtain the tuning curve. We used the motion direction tuning curve to adjust the peak firing rate of the spiking response according to the jitter in the preferred direction alignment.

We simulated the DSGC population response to a moving edge traveling from left to right at a constant speed of 330 μm/second. To simulate the occlusion protocol, we introduced an occlusion placed over a left motion-preferring DSGC whose position in space was fixed (approximately the 50th left motion-preferring DSGC). For each spatial arrangement of DSGCs, the simulation was repeated 100 times. The spiking response of each DSGC was discretized in time. At each 25-ms time bin, the firing rate given by the rectified sine wave fit was converted to a mean spike count. The number of spikes generated by a DSGC was obtained by sampling from a Gaussian distribution with this mean and a sub-Poisson, constant variance of 0.4. The sub-Poisson noise was determined from our experimental data by analyzing the variance of the spiking responses to 6 repetitions of the full-field moving bar (10 cells) and the occlusion stimulus (9 cells) (Figure S7D). The spatial positions of the DSGCs were shuffled in each simulation block for a total of 1000 blocks with 100 repetitions in each block.

A population vector (Dayan and Abbott, 2001) was used to decode the spatial position of the moving bar's leading edge. The position estimate $\hat{x}$ at a given time was the firing rate-weighted average of DSGCs' spatial positions

$$\hat{x} = \frac{\sum_i r_i \tilde{x}_i}{\sum_i r_i}$$

where r_i is the firing rate of the ith cell and $\tilde{x}_i \sim \mathcal{N}(x_i, {w_i}^2)$ where x_i is the soma position and w_i the RF width of the ith cell. The RF width was taken to be the 1 SD boundary of the Gaussian center profile (Chichilnisky and Kalmar, 2002). RF widths were obtained by scaling the dendritic field radii by 1.25. Dendritic field radii were obtained by sampling from Gaussian distribution with $\mu = 88$ μm and $\sigma = 14.8$ μm. In the population vector decoder, we added 130 μm to the soma position of the occluded DSGC to compensate

for the lag of the null-direction response to the occlusion stimulus. Errors are reported as the root mean-square-error in the position estimate (Figure 7E).

References

Barlow, H. B. & Hill, R. M. (1963). Selective sensitivity to direction of movement in ganglion cells of rabbit retina. *Science* **139**, 412–414.

Barlow, H.B., and Levick, W.R. (1965). The mechanism of directionally selective units in rabbit's retina. *J. Physiol*. **178**, 477–504.

Briggman, K.L., Helmstaedter, M., and Denk, W. (2011). Wiring specificity in the direction-selectivity circuit of the retina. *Nature* **471**, 183–188.

Chen, Q., Pei, Z., Koren, D., and Wei, W. (2016). Stimulus-dependent recruitment of lateral inhibition underlies retinal direction selectivity. *Elife* **5**, e21053.

Chiao, C.C., and Masland, R.H. (2003). Contextual tuning of direction-selective retinal ganglion cells. *Nat. Neurosci*. **6**, 1251–1252.

Chichilnisky, E.J. and Kalmar, R.S. (2002). Functional asymmetries in ON and OFF ganglion cells of primate retina. *J. Neurosci.* **22**, 2737–2747.

Cruz-Martín, A., El-Danaf, R.N., Osakada, F., Sriram, B., Dhande, O.S., Nguyen, P.L., Callaway, E.M., Ghosh, A., and Huberman, A.D. (2014). A dedicated circuit links direction-selective retinal ganglion cells to the primary visual cortex. *Nature* **507**, 358–361.

Dayan, P. and Abbott, L. (2001). Theoretical neuroscience - computational and mathematical modeling of neural systems. Cambridge, MA: MIT Press.

Demb, J. B., Haarsma, L., Freed, M. A. and Sterling, P. (1999). Functional circuitry of the retinal ganglion cell's nonlinear receptive field. *J. Neurosci.* **19**, 9756–9767.

Deny, S., Ferrari, U., Macé, E., Yger, P., Caplette, R., Picaud, S., Tkačik, G., and Marre, O. (2017). Multiplexed computations in retinal ganglion cells of a single type. *Nat. Commun.* **8**, 1964.

1007 Dhande, O.S., Stafford, B.K., Lim, J.-H.A., and Huberman, A.D. (2015). Contributions of
1008 retinal ganglion cells to subcortical visual processing and behaviors. *Annu. Rev. Vis.*
1009 *Sci.* **1**, 291–328.
1010
1011 Ding, H., Smith, R.G., Poleg-Polsky, A., Diamond, J.S., and Briggman, K.L. (2016).
1012 Species-specific wiring for direction selectivity in the mammalian retina. *Nature* **535**,
1013 105–110.
1014
1015 Ellis, E.M., Gauvain, G., Sivyer, B., and Murphy, G.J. (2016). Shared and distinct retinal
1016 input to the mouse superior colliculus and dorsal lateral geniculate nucleus. *J.*
1017 *Neurophysiol.* **116***,* 602–610.
1018
1019 Euler, T., Detwiler, P. B. and Denk, W. (2002). Directionally selective calcium signals in
1020 dendrites of starburst amacrine cells. *Nature* **418**, 845–852.
1021
1022 Famiglietti, E. V. (1983). “Starburst” amacrine cells and cholinergic neurons: mirror-
1023 symmetric ON and OFF amacrine cells of rabbit retina. *Brain Res.* **261**, 138–144.
1024
1025 Fiscella, M., Franke, F., Farrow, K., Müller, J., Roska, B., da Silveira, R.A., and
1026 Hierlemann, A. (2015). Visual coding with a population of direction-selective neurons. *J.*
1027 *Neurophysiol.* **114**, 2485–2499.
1028
1029 Franke, K., Berens, P., Schubert, T., Bethge, M., Euler, T., and Baden, T. (2017).
1030 Inhibition decorrelates visual feature representations in the inner retina. *Nature* **542**,
1031 439–444.
1032
1033 Fried, S.I., Münch, T.A., and Werblin, F.S. (2002). Mechanisms and circuitry underlying
1034 directional selectivity in the retina. *Nature* **420**, 411–414.
1035
1036 Grzywacz, N.M., and Amthor, F.R. (2007). Robust directional computation in on-off
1037 directionally selective ganglion cells of rabbit retina. *Vis. Neurosci.* **24**, 647–661.
1038
1039 He, S., Jin, Z.F., and Masland, R.H. (1999). The nondiscriminating zone of directionally
1040 selective retinal ganglion cells: comparison with dendritic structure and implications for
1041 mechanism. *J. Neurosci.* **19**, 8049–8056.
1042
1043 He, S., and Masland, R.H. (1998). ON direction-selective ganglion cells in the rabbit
1044 retina: Dendritic morphology and pattern of fasciculation. *Vis. Neurosci.* **15**, 369–375.
1045

1046 Huang, X., Rangel, M., Briggman, K.L., and Wei, W. (2019). Neural mechanisms of
1047 contextual modulation in the retinal direction selective circuit. *Nat. Commun.* **10**, 2431.
1048
1049 Huberman, A.D., Wei, W., Elstrott, J., Stafford, B.K., Feller, M.B., and Barres, B.A.
1050 (2009). Genetic identification of an On-Off direction- selective retinal ganglion cell
1051 subtype reveals a layer-specific subcortical map of posterior motion. *Neuron* **62**, 327–
1052 334.
1053
1054 Ishikane, H., Gangi, M., Honda, S., Tachibana, M. (2005). Synchronized retinal
1055 oscillations encode essential information for escape behavior in frogs. *Nat.*
1056 *Neurosci.* **8**, 1087–1095.
1057
1058 Ito, S., and Feldheim, D.A. (2018). The mouse superior colliculus: An emerging model
1059 for studying circuit formation and function. *Front. Neural Circuits* **12**, 10.
1060
1061 Jacoby, J. and Schwartz, G.W. (2017). Three small-receptive-field ganglion cells in the
1062 mouse retina are distinctly tuned to size, speed, and object motion. *J Neurosci.* **37**, 610–625.
1063
1064 Kay, J.N., de la Huerta, I., Kim, I.J., Zhang, Y., Yamagata, M., Chu, M.W., Meister, M.,
1065 and Sanes, J.R. (2011). Retinal ganglion cells with distinct directional preferences differ
1066 in molecular identity, structure, and central projections. *J. Neurosci.* **31**, 7753–7762.
1067
1068 Kim, T., Soto, F., and Kerschensteiner, D. (2015). An excitatory amacrine cell detects
1069 object motion and provides feature-selective input to ganglion cells in the mouse retina.
1070 *Elife* **4**, e08025.
1071
1072 Kittila, C.A., and Massey, S.C. (1997). Pharmacology of directionally selective ganglion
1073 cells in the rabbit retina. *J. Neurophysiol.* **77**, 675–689.
1074
1075 Kühn, N.K., and Gollisch, T. (2019). Activity correlations between direction-selective
1076 retinal ganglion cells synergistically enhance motion decoding from complex visual
1077 scenes. *Neuron* **101**, 963–976.
1078
1079 Lee, S., Kim, K., and Zhou, Z.J. (2010). Role of ACh-GABA cotransmission in detecting
1080 image motion and motion direction. *Neuron* **51**, 787–799.
1081
1082 Lee, S., Zhang, Y., Chen, M., and Zhou, Z.J. (2016). Segregated glycine-glutamate co-
1083 transmission from vGluT3 amacrine cells to contrast-suppressed and contrast-
1084 enhanced retinal circuits. *Neuron* **90**, 27–34.
1085

Levakova, M., Tamborrino, M., Ditlevsen, S., and Lansky, P. (2015). A review of the methods for neuronal response latency estimation. *Biosystems* **136**, 23–34.

Lipin, M.Y., Rowl Taylor, W., and Smith, R.G. (2015). Inhibitory input to the direction-selective ganglion cell is saturated at low contrast. *J. Neurophysiol.* **114**, 927–941.

Marre, O., Botella-Soler, V., Simmons, K.D., Mora, T., Tkačik, G., and Berry, M.J. (2015). High accuracy decoding of dynamical motion from a large retinal population. *PLoS Comput. Biol.* **11**, e1004304.

Matsumoto, A., Briggman, K.L., and Yonehara, K. (2019). Spatiotemporally asymmetric excitation supports mammalian retinal motion sensitivity. *Curr. Biol.* **29**, 3277–3288.

Ölveczky, B. P., Baccus, S. A. and Meister, M. (2003). Segregation of object and background motion in the retina. *Nature* **423**, 401–408.

Oyster, C.W., and Barlow, H.B. (1967). Direction-selective units in rabbit retina: Distribution of preferred directions. *Science* **155**, 841–842.

Rivlin-Etzion M., Zhou K., Wei W., Elstrott J., Nguyen P.L., Barres B.A., Huberman A.D., and Feller M.B. (2011). Transgenic mice reveal unexpected diversity of On-Off direction-selective retinal ganglion cell subtypes and brain structures involved in motion processing. *J Neurosci.* **31**, 8760–8769.

Rousso, D.L.L., Qiao, M., Kagan, R.D.D., Yamagata, M., Palmiter, R.D.D., and Sanes, J.R.R. (2016). Two pairs of ON and OFF retinal ganglion cells are defined by intersectional patterns of transcription factor expression. *Cell Rep*. **15**, 1930–1944.

Sabbah, S., Gemmer, J.A., Bhatia-Lin, A., Manoff, G., Castro, G., Siegel, J.K., Jeffery, N., and Berson, D.M. (2017). A retinal code for motion along the gravitational and body axes. *Nature* **546**, 492–497.

Sanes, J.R. and Masland R.H. (2015). The types of retinal ganglion cells: current Status and implications for neuronal classification. *Ann. Rev. Neurosci.* **38**, 221–246.

Schwartz, G., Taylor, S., Fisher, C., Harris, R., and Berry, M.J., II (2007). Synchronized firing among retinal ganglion cells signals motion reversal. *Neuron* **55**, 958–969.

1124 Sethuramanujam, S., McLaughlin, A.J., deRosenroll, G., Hoggarth, A., Schwab, D.J.,
1125 and Awatramani, G.B. (2016). A central role for mixed acetylcholine/GABA transmission
1126 in direction coding in the retina. *Neuron* **90**, 1243–1256.
1127
1128 Sivyer, B., van Wyk, M., Vaney, D.I., and Taylor, W.R. (2010). Synaptic inputs and
1129 timing underlying the velocity tuning of direction-selective ganglion cells in rabbit retina.
1130 *J. Physiol.* **588**, 3243–3253.
1131
1132 Shi, X., Barchini, J., Ledesma, H.A., Koren, D., Jin, Y., Liu, X., Wei, W., and Cang, J.
1133 (2017). Retinal origin of direction selectivity in the superior colliculus. *Nat. Neurosci.* **20**,
1134 550–558.
1135
1136 Spruston, N. (2008). Pyramidal neurons: dendritic structure and synaptic integration.
1137 *Nat. Neurosci. Reviews* **9**, 206–221.
1138
1139 Takeshita, D., and Gollisch, T. (2014). Nonlinear spatial integration in the receptive field
1140 surround of retinal ganglion cells. *J. Neurosci.* **34**, 7548–7561.
1141
1142 Taylor, W.R., and Vaney, D.I. (2002). Diverse synaptic mechanisms generate direction
1143 selectivity in the rabbit retina. *J. Neurosci.* **22**, 7712–7720.
1144
1145 Trenholm, S., Johnson, K., Li, X., Smith, R.G., and Awatramani, G.B. (2011). Parallel
1146 mechanisms encode direction in the retina. *Neuron* **71**, 683–694.
1147
1148 Turner, M.H., Schwartz, G.W., and Rieke, F. (2018). Receptive field center-surround
1149 interactions mediate context-dependent spatial contrast encoding in the retina. *Elife* **7**,
1150 e38841.
1151
1152 Wei, W., Hamby, A.M., Zhou, K., and Feller, M.B. (2011). Development of asymmetric
1153 inhibition underlying direction selectivity in the retina. *Nature* **469**, 402–406.
1154
1155 Wyatt, H.J., and Daw, N.W. (1975). Directionally sensitive ganglion cells in the rabbit
1156 retina: specificity for stimulus direction, size and speed. *J. Neurophysiol.* **38**, 613–626.
1157
1158 Yonehara, K., Balint, K., Noda, M., Nagel, G., Bamberg, E., and Roska, B. (2011).
1159 Spatially asymmetric reorganization of inhibition establishes a motion-sensitive circuit.
1160 *Nature* **469**, 407–410.
1161

1162 Zhang, Y., Kim, I.J., Sanes, J.R., and Meister, M. (2012). The most numerous ganglion
1163 cell type of the mouse retina is a selective feature detector. *Proc. Natl. Acad. Sci. U. S.*
1164 *A.* **109**, E2391–E21398.
1165
1166 Zylberberg, J., Cafaro, J., Turner, M.H., Shea-Brown, E., and Rieke, F. (2016).
1167 Direction-selective circuits shape noise to ensure a precise population code. *Neuron* **89**,
1168 369–383.
1169